



Understanding high-temperature corrosion behavior of an AlN/Mo functionally graded material exposed to Li/LiF-LiCl-LiBr vapor

Mingyong Jia ^{a,b}, Fei Chen ^{a,c,*}, Xipeng Tan ^b, Yaling He ^d, Yueqi Wu ^a, Qiang Shen ^a

^a State Key Laboratory of Advanced Technology for Materials Synthesis and Processing, Wuhan University of Technology, Wuhan 430070, China

^b Department of Mechanical Engineering, National University of Singapore, 9 Engineering Drive 1, Singapore 117575, Singapore

^c Hubei Longzhong Laboratory, Xiangyang 441000, Hubei, China

^d State Key Laboratory of Advanced Electromagnetic Engineering and Technology, Huazhong University of Science and Technology, Wuhan 430074, China



ARTICLE INFO

Keywords:

Liquid metal battery
Li/LiF-LiCl-LiBr vapor
Corrosion
AlN ceramics
Functionally graded materials

ABSTRACT

The high-temperature corrosion behavior of an AlN/Mo functionally graded material (FGM) under the Li/LiF-LiCl-LiBr vapor has been investigated. It is suggested that the Li vapor diffuses along the AlN and AlN/Mo grain boundaries and enters the interior of adjacent AlN grains, leading to the disintegration of AlN grains and subsequent failures. The 3D Mo networks are barely corroded, thus preventing cracking that may occur due to the inconsistent deformation inside the FGM. This work unravels the high-temperature corrosion mechanisms for the AlN/Mo FGM. Meanwhile, the operating temperature threshold for the liquid metal batteries employing Mo/AlN/Mo seals is determined to be ~ 600 °C.

1. Introduction

Liquid metal battery (LMB) is an emerging solution for the large-scale grid energy storage, which consists of two liquid metal electrodes separated by a molten salt electrolyte. The positive electrode, negative electrode, and molten salt electrolyte self-segregate into three layers at operating temperature because of density and immiscibility [1–4]. The electrochemical reaction between metal A and metal B provides the driving force for the LMB. In the discharge process, metal A is electrochemically oxidized ($A \rightarrow A^{n+} + ne^-$), which reduces the thickness of the negative electrode layer. The cations are conducted through the molten salt electrolyte towards the positive electrode while the electrons are released to the external circuit. Concurrently, the thickness of the positive electrode layer increases from the cations being electrochemically reduced to form a liquid A-B alloy ($A^{n+} + ne^- \rightarrow A$ (in B)). This process is reversed during charging [3,5]. The batteries composed of Li||Sb-Pb electrodes and LiF-LiCl-LiBr electrolyte (22:31:47 mol%) are considered to be one of the most promising LMBs largely due to the favorable cost, voltage, operating temperature, and energy efficiency [3, 6,7]. However, LMBs are usually sensitive to oxygen and moisture at operating temperatures due to the active Li vapor and the spontaneous reaction between the sealing materials and the electrode materials, and gradually decay or fail once exposed to air [8]. At operating

temperatures above 300 °C, no polymer currently suits for the long-time sealing application. Therefore, it is a big challenge to realize a LMB with the hermetic sealing, electrical insulation, chemical stability, and high-temperature stability simultaneously [9,10]. The Na-S batteries with liquid metal electrodes can be cycled for more than 15 years at a temperature of 350 °C, using Al-Al₂O₃-Al or glass-ceramic as sealing and insulation components [11,12]. However, when applying the same components to Li-based LMBs, the challenge lies in the Li, which can spontaneously reduce the Al₂O₃ to Al, leading to a seal failure. The low thermal stability of the glass-ceramic also leads to battery electrode leakage [8].

The primary internal environment of LMBs is the Li/LiF-LiCl-LiBr vapor, and its internal pressure is about three times than the standard atmospheric pressure at 500 °C. The phenomenon of high-temperature molten salt vapor corrosion is not exclusive to LMBs [13,14]. Ceramics are an ideal type of sealing materials compared to the metals of poor insulators as well as the polymers that cannot withstand high-temperature conditions. Nagura et al. [15] studied the corrosion resistance of insulating ceramic materials in a natural convection lithium loop. They found that AlN and Er₂O₃ ceramics remained initial surface conditions at 500 °C, and Y₂O₃ ceramics were corroded due to the formation of LiYO₂. Wang et al. [16] investigated the corrosion behavior of ceramic candidates for tritium permeation barriers exposed

* Corresponding author at: State Key Laboratory of Advanced Technology for Materials Synthesis and Processing, Wuhan University of Technology, Wuhan 430070, China.

E-mail address: chenfei027@whut.edu.cn (F. Chen).

to molten lithium. It was indicated that AlN, SiC, and Er_2O_3 ceramics showed substantial stability with liquid lithium through thermodynamic simulations and static compatibility tests. While AlN demonstrated better thermodynamic stability with lithium at high temperatures than oxide ceramics [17–19]. Based on the high-temperature stability, insulation, and compatibility, AlN ceramics are one of the most potential materials for battery insulators. There are still limited researches that are conducted to investigate the corrosion resistance of AlN ceramics in LMBs. Li et al. [20] studied the corrosion behavior and mechanism of lithium vapor on AlN ceramics and revealed that the failure mechanism of AlN in Li vapor is closely related to the reactions between Li and the second phase (yttrium-aluminum compounds) on the grain boundaries. Zhang et al. [21] analyzed the corrosion behavior of AlN ceramics in the LiF-LiCl-LiBr-Li molten salt with different Li concentrations and found that the Al_2O_3 layer on the surface of the AlN grain plays a crucial role in inhibiting the corrosion reaction between Li and $\text{Y}_3\text{Al}_5\text{O}_{12}$ and preventing the destruction of AlN ceramics.

In addition to the desirable properties of ceramics (corrosion resistance, electrical insulation, thermal stability, etc.), the corrosion resistance of the joint between the ceramic and battery case in the sealing component could directly affect the function of the LMBs [8]. Due to the distinct physical and chemical properties for ceramics and metals, the metallization of AlN ceramics remains challenging for some reasons such as bond types, thermal expansion coefficients, wetting angles, and brittle interfacial phases [22,23]. Conventional laminated composites consisting of ceramics and metals have problems with delamination, often occurring at the joining interface due to the thermal stresses induced by the differences in physical properties. The Li/LiF-LiCl-LiBr vapor leaking from the interface of ceramic/metal leads to a gradual decrease in battery efficiency until a complete failure. To solve this issue, functionally graded materials (FGMs) were used to achieve symmetrical graded surface metallization of the AlN ceramic, which was then welded to the battery case [24,25]. By using the strategy of gradient axial compositions, the interface-free joining of AlN and Mo was realized, and the residual thermal stresses were significantly reduced [26,27]. Notably, the minimum operating temperatures of the LMBs depended on the melting points of the electrodes and the salt electrolyte, which are usually higher than 400 °C [3]. It is of great significance to investigate the corrosion resistance of the Mo/AlN/Mo FGMs under elevated temperatures and variable temperature vapor of the electrodes and the molten salt electrolyte, considering that the sealing component is the weakest part in the battery packaging structure. Therefore, the high-temperature corrosion behavior of the AlN/Mo FGMs composed of the AlN layer and AlN/Mo graded layers under varying temperatures was investigated, including structural deformation, phase transition, and spatial corrosion depth. Particularly, the

operating temperature driven corrosion mechanisms for the AlN/Mo FGMs under the Li/LiF-LiCl-LiBr vapor are unraveled.

2. Experimental

2.1. Materials

In this work, an experimental corrosion setup as illustrated in Fig. 1(a) was built for simulating the real operating environment of the LMBs composed of Li||Sb-Pb electrodes and LiF-LiCl-LiBr electrolyte, in which corrosive environment includes Li vapor, LiF-LiCl-LiBr vapor, anhydrous, oxygen-free, and high temperatures is involved.

AlN ceramics, AlN/Mo composites (1:1 vol%), and AlN/Mo graded materials were used to investigate the high-temperature corrosion behavior. The AlN/Mo FGMs used in this work were composed of AlN ceramic, AlN/Mo graded composites, and Mo. Commercially available powder of AlN (Tokuyama Corporation, Tokyo, Japan, 1 μm; purity ≥99.99 wt%) and Mo (Aladdin Inc., Shanghai, China, 10 μm; purity ≥99.5 wt%) were used as the raw powder materials. Y_2O_3 powder (Aladdin Inc., Shanghai, China, 2–5 μm; purity ≥99.99 wt%) of 3 wt% was used as the sintering aid to reduce the sintering temperature of AlN ceramics. AlN and Mo powders were fully mixed in various volume ratios covering the range from 100 % AlN to 100 % Mo at 20 % intervals and manually layered in the graphite mold and pre-pressed before sintering. Previous studies have systematically explored the sintering process of AlN/Mo FGMs [26,27]. Strip specimens were cut into a dimension of 20 mm × 4 mm × 3 mm and then ground until 3000# SiC paper before the corrosion experiment.

2.2. Li/LiF-LiCl-LiBr vapor corrosion tests

The corrosion process was replicated as close to the real operating conditions of the 20 Ah LMBs. LiF-LiCl-LiBr (22:31:47 mol%) salts were firstly mixed using the commercially available LiF, LiCl, and LiBr (Aladdin Inc., Shanghai, China; purity ≥99.5 wt%) and then dried at 160 °C in the oven for 12 h to eliminate moisture. The 304 L stainless steel container (see Fig. 1(b)) holding specimens, mixed salts (120 g), and Li metal (Aladdin Inc., Shanghai, China; purity ≥99.5 wt%, 6 g) was sealed by graphite ring and screw to create a relatively stable Li/LiF-LiCl-LiBr vapor environment. The nickel foam was used to separate the specimens from Li/LiF-LiCl-LiBr to ensure that the specimens did not contact high-temperature molten salts and liquid metal during the corrosion experiment. Finally, the assembled and sealed experimental setup were placed in the oven and heated to 550 °C, 600 °C, 650 °C, 700 °C, and 750 °C, respectively, at a heating rate of 10 °C/min, and then cooled to room temperature after 100 h. It should be noted that all

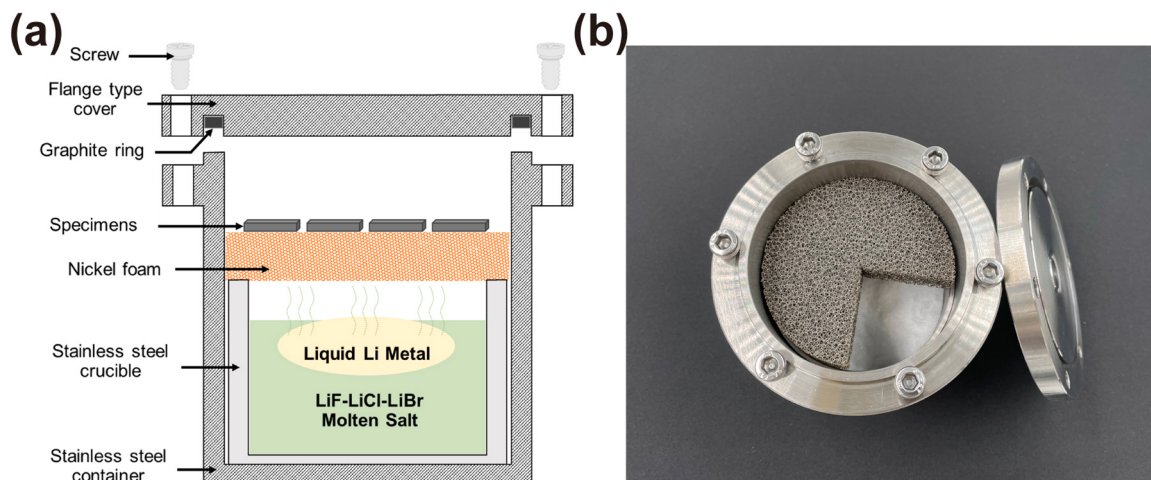


Fig. 1. (a) Schematic diagram and (b) photo of dynamic vapor corrosion experimental device.

corrosion experiments were conducted in a high-purity Ar atmosphere glove box in which H_2O and O_2 were maintained below 0.01 and 0.01 ppm, respectively. After Li/LiF-LiCl-LiBr vapor corrosion tests, the specimens were taken out of the stainless steel container and glove box and kept in vacuum bags until removal for detailed characterization.

2.3. Characterization methods

The bending strength of the AlN ceramics and AlN/Mo composites specimens with dimensions: 20 mm × 4 mm × 3 mm was measured at room temperature via a universal testing machine (INSTRON, Instron 5566, Norwood, USA). X-ray diffractometer with CuK α radiation (XRD; PANALYTICAL Empyrean, Netherlands) was used to analyze the phase composition of the specimens before and after Li/LiF-LiCl-LiBr vapor corrosion. The surface morphology and microstructure of the specimens were observed using a field emission scanning electron microscope (FESEM; Zeiss Ultra Plus, Germany). The corrosion depth in the radial direction and the elements distribution of the specimens were examined by an electron probe microanalyzer (EPMA; JEOL, JXA-8230, Tokyo, Japan). In addition, thin lamellas of the region of interest in corroded specimens were prepared by the focused ion beam (FIB; FEI Helios Nanolab, America) and characterized using transmission electron microscopy (TEM; FEI Talos F200, America) equipped with selected-area electron diffraction and energy-dispersive X-ray spectroscopy (EDS). Precise characterization of phase composition, microstructural morphology, and mechanical properties were individually applied to AlN ceramics and AlN/Mo composites, respectively, to evaluate the corrosion behavior of AlN/Mo graded materials. The simultaneous

corrosion of high-temperature vapor parallel to each graded layer in the liquid metal battery, instead of only on the terminal AlN or Mo layers, which confirms the feasibility of our strategy.

3. Results and discussion

3.1. Weight-gain analysis and macroscopic observation

Fig. 2 shows the weight variations and macroscopic observations of the AlN/Mo FGMs, the AlN layer, and the AlN/Mo layer after an exposure to the Li/LiF-LiCl-LiBr vapor at varied temperatures for 100 h. With the temperature increase from 550 °C to 750 °C, as shown in **Fig. 2(b)**, white bubble-shaped corrosion products appeared on the surface of each specimen, increasing the specimen weight. The weight gain trend for the AlN/Mo FGMs, the AlN layer, and the AlN/Mo layer is consistent, as shown in **Fig. 2(a)**, of which 650 °C is a significant turning point. When the temperature is lower than 650 °C, there is no obvious change in weight (less than 1 mg/cm²) and geometry on the surface of each specimen. The weight gain rate (WGR) is used to show the weight gain degree of the specimen under different corrosion temperatures [28]. It is shown that the weight gain rate of the AlN/Mo FGMs, the AlN layer, and the AlN/Mo layer increases dramatically from 600 °C to 650 °C, which is approximately 440 %, 450 %, and 400 %, respectively. With the rapid increase in weight gains, the bending strengths of the AlN and AlN/Mo layers drop obviously (**Fig. 2(a)**). Particularly, a severe distortion of the AlN/Mo FGMs after corrosion at 750 °C is manifested as the outer expansion of the AlN layer, the delamination of the graded layers, and the two ~18.5° symmetrical angles formed in-between the AlN layer

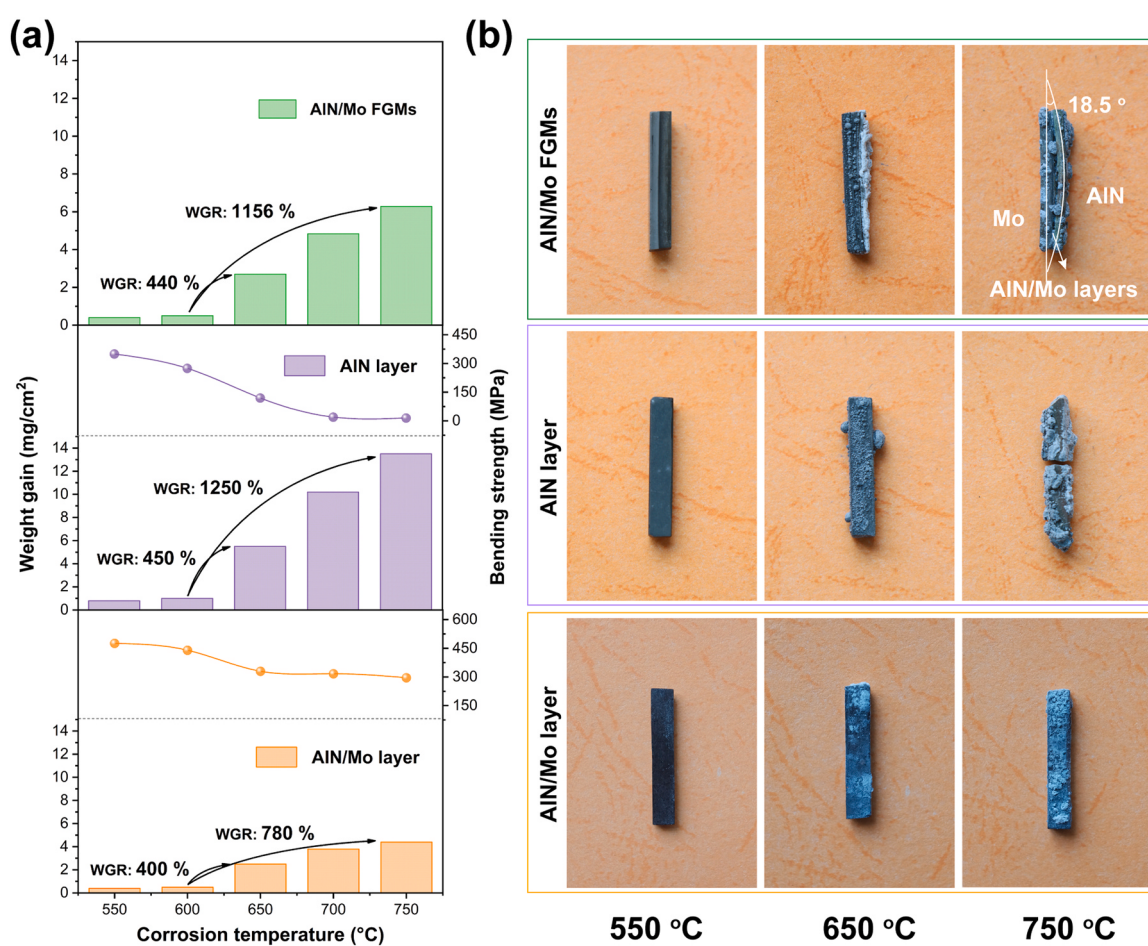


Fig. 2. (a) weight variations and (b) macroscopic observations of the AlN layer, the AlN/Mo layer, and AlN/Mo FGMs after exposure to Li/LiF-LiCl-LiBr vapor at different temperatures for 100 h.

and the Mo layer.

In general, high operating temperatures lead to a high vapor pressure of liquid metals and electrolytes, and more serious corrosion issues [8]. The increased activity of the Li/LiF-LiCl-LiBr vapor and the adhesion during cooling cause specimens to gain weight with the higher corrosion temperature. However, it is indicated that the WGR is closely related to the materials type and the corrosion process, but not merely to the temperature. The WGR of the AlN/Mo layer is ~780 % from 600 °C to 750 °C, which is lower than that of the AlN/Mo FGMs and the AlN layer, indicating that Mo inhibits the corrosion progress or adhesion during cooling of the Li/LiF-LiCl-LiBr vapor on the specimens. The AlN/Mo layer is found to be distortion-free and still maintains a bending strength of ~296.3 MPa after exposure to the Li/LiF-LiCl-LiBr vapor at 750 °C for 100 h. Regrettably, there is currently no established testing standard for evaluating the bending strength of FGMs, and a consistent value for the bending strength of such materials cannot be defined. This variability arises from factors like the magnitude of the gradient variation, interface morphology, and the direction of testing.

3.2. Corrosion processes and the products

Fig. 3 shows the XRD patterns of the AlN layer and the AlN/Mo layer after exposure to the Li/LiF-LiCl-LiBr vapor at varied temperatures for 100 h. It is suggested that the reaction processes of the AlN layer and the AlN/Mo layer are divided into two stages with the increase of the corrosion temperatures, and 650 °C is the turning point. As shown in **Fig. 3(a)**, the peaks of YAlO₃ induced by the 3 wt% Y₂O₃ sintering

additives transforms to the peaks of Li₅AlO₄ with the temperature increase from 600 °C to 650 °C. The LiOH gradually is enriched from 650 °C, and is almost the only secondary phase on the surface of the AlN layer at 750 °C. Unlike the AlN layer, no YAlO₃ peaks are observed in the AlN/Mo layer (**Fig. 3(b)**). Only the AlN and Mo phases are detectable on the surface of the AlN/Mo layer after corrosion at 550 °C and 600 °C. The LiOH appears from 650 °C to 750 °C, and the peaks of Li₅AlO₄ are detected as the temperature reaches 700 °C.

The XRD analysis results show that no halides (like LiF, LiCl, and LiBr) are formed on the surface of the specimens, meaning that they were not involved in the corrosion under an amorphous state. Therefore, the corrosion of the AlN/Mo FGMs at elevated temperatures is dominated by the Li vapor. Due to the strong covalent bonding, rare-earth and alkaline-earth oxides are often added as sintering additives in the fabrication of AlN ceramics to reduce the sintering temperature and achieve a fully density [29–31]. Y₂O₃ is the most effective additive to react with Al₂O₃ inherited from the AlN powder surface, thus forming a eutectic liquid that promotes AlN densification at a lower temperature [32,33]. The secondary phases in the AlN ceramics with Y₂O₃ can be Y₃Al₅O₁₂ (YAG), YAlO₃ (YAP), and Y₄Al₂O₉ (YAM), which is related to the Y₂O₃/Al₂O₃ ratio and the sintering temperature. Only the YAlO₃ (YAP) is detected as the secondary phase on the grain boundary of the AlN ceramics in this study, and the reaction is suggested as follows [33]:



According to the thermodynamic calculations, AlN and Y₂O₃ present

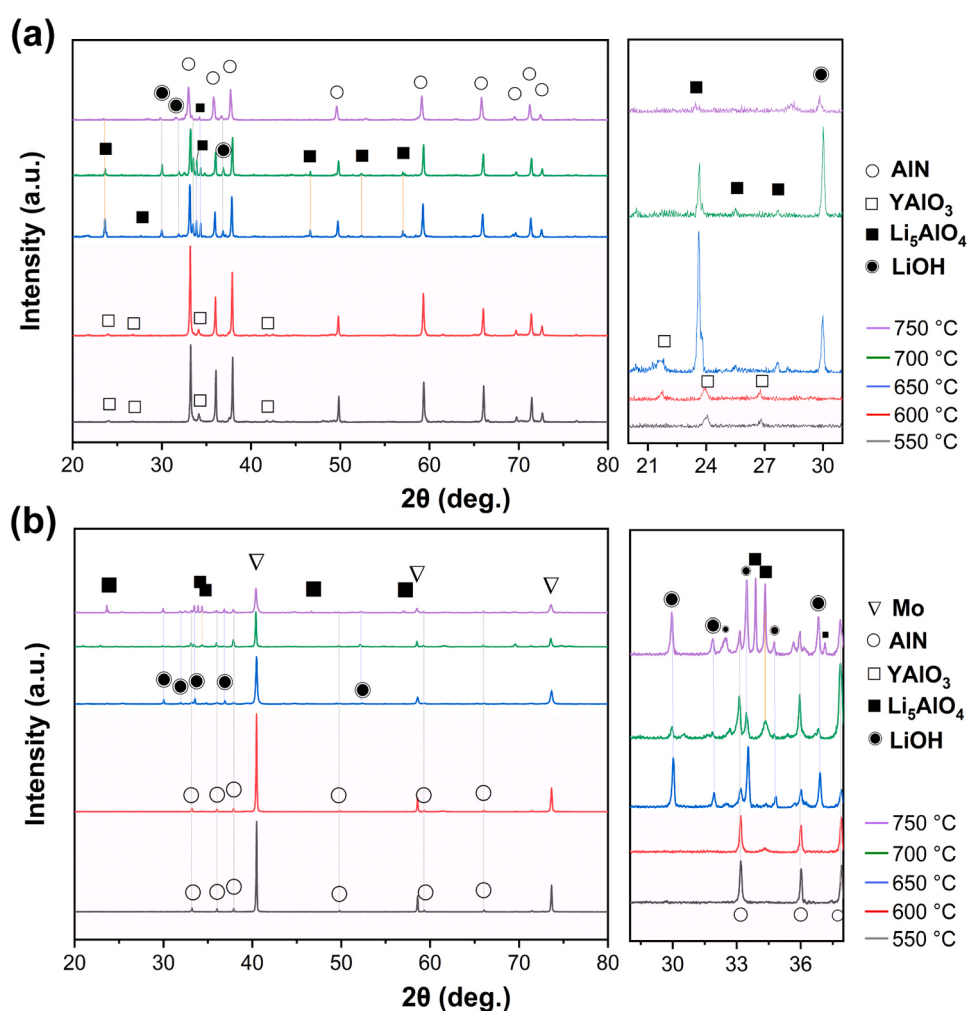
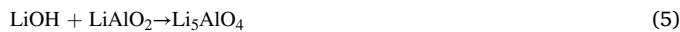
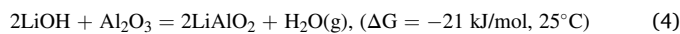
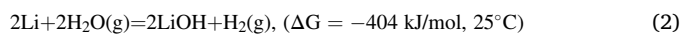


Fig. 3. XRD patterns of (a) AlN layer, (b) AlN/Mo layer after exposure to the Li/LiF-LiCl-LiBr vapor at different temperatures for 100 h.

high stability with strongly reducing liquid Li within the possible operating temperatures of LMBs, i.e. $3\text{Li} + \text{AlN} \rightarrow \text{Li}_3\text{N} + \text{Al}$, ($\Delta G = 175 \text{ kJ/mol}$, 550°C), and $6\text{Li} + \text{Y}_2\text{O}_3 \rightarrow 3\text{Li}_2\text{O} + 2\text{Y}$, ($\Delta G = 194 \text{ kJ/mol}$, 550°C). The corrosion products LiOH and Li_5AlO_4 on the surface of the specimens are formed during the test in air and corrosion reaction, respectively, due to the experiment being conducted in a high-purity Ar atmosphere glove box. During the test, Li adhering to the specimens is in contact with air, reacting rapidly with oxygen and water to generate LiOH and release hydrogen, i.e. $4\text{Li} + \text{O}_2(\text{g}) = 2\text{Li}_2\text{O}$, ($\Delta G = -1123 \text{ kJ/mol}$, 25°C), $\text{Li}_2\text{O} + \text{H}_2\text{O}(\text{g}) = 2\text{LiOH}$, ($\Delta G = -80 \text{ kJ/mol}$, 25°C), and $2\text{Li} + 2\text{H}_2\text{O}(\text{g}) = 2\text{LiOH} + \text{H}_2(\text{g})$, ($\Delta G = -404 \text{ kJ/mol}$, 25°C). Several studies have reported the spontaneous reaction of strongly reducing Li with the secondary phase caused by sintering additives, implying that the Li_5AlO_4 detected in XRD is obtained by the reaction of Li and YAlO_3 [15,20,21]. In addition, the fraction of YAlO_3 in the AlN/Mo layer is too low to transform into the detectable Li_5AlO_4 , as shown in Fig. 3(b). Combined with the phases in the AlN/Mo layer and the oxide layer on the surface of AlN grains [29,33], it is speculated that the excess Li_5AlO_4 is formed by the multi-steps reaction between Li and Al_2O_3 (Eqs. (2–5)):



Where ΔG is the standard Gibbs free energy of the reaction, calculated by the HSC Chemistry 9.0 software.

The surface morphologies of the AlN layer and AlN/Mo layer before and after exposure to the Li/LiF-LiCl-LiBr vapor at varied temperatures for 100 h are shown in Figs. 4 and 5. It is seen that the AlN grains and grain boundaries are visible before corrosion, and the average grain size is $\sim 2 \mu\text{m}$. With the temperature increase from 550°C to 750°C , heterogeneous particles gradually adhere to the surface of AlN grains until the AlN matrix is completely obscured. When the temperature is 550°C and 600°C , only a small amount of nano-scale spherical and elliptical heterogeneous particles adheres to the surface of AlN respectively, which leads to a slight gain in the weight of specimens, as shown in Fig. 4(b) and (c) and Fig. 2. However, the heterogeneous particles are

not detected in the XRD patterns due to their low quantity or amorphous state in nature. When the temperature reaches 650°C , large heterogeneous particles (~ 10 and $60 \mu\text{m}$) adhere to the surface of AlN, resulting in a rapid increase in the weight after the corrosion test, as shown in Fig. 4(d) and Fig. 2. The XRD patterns in Fig. 3(a) shows that the tiled spherical heterogeneous particles are LiOH . As the corrosion temperature increases to 750°C , the large-scale LiOH ($\sim 60 \mu\text{m}$) disintegrates and transforms into a network evenly spread on the surface of AlN. The morphology evolution of the AlN/Mo layer is akin to that of the AlN layer. The corrosion process on the surface of the AlN/Mo layer is much slower than that of the AlN layer due to the spatial framework barrier and excellent corrosion resistance of Mo. The AlN and Mo grains are visible after corrosion at 550°C , as shown in Fig. 5(b). Only a small amount of nano-scale spherical heterogeneous particles are grown on the AlN grains after corrosion at 600°C , as shown in Fig. 5(c). With the temperature increase from 650°C to 750°C , heterogeneous particles appear on the surface of the AlN/Mo layer, together with the formation and disintegration of large-scale particles, as shown in Fig. 5(d-f). The XRD patterns in Fig. 3(b) also show that the heterogeneous spherical particles are LiOH .

3.3. Spatial corrosion depth analysis

The high-temperature corrosion of AlN/Mo FGMS under the Li/LiF-LiCl-LiBr vapor occurs on both AlN and AlN/Mo layers. The analysis of spatial corrosion depth for the AlN and the AlN/Mo layers provides an insight into the corrosion mechanism. EPMA was employed to quantitatively examine the elemental distributions of Al, Mo, O, and Br on the cross-section of the corroded AlN and AlN/Mo layers respectively, as shown in Figs. 6 and 7. After the corrosion at 550°C and 600°C for 100 h, no visible changes take place on the AlN layer (Fig. 6(b) and (c)), indicating that there should be no corrosion inside the AlN layer yet. However, with the temperature rising from 600°C to 750°C , the elemental concentration on the cross-section fluctuates and cracks appear (Fig. 6(d-f)). The intergranular corrosion and volume expansion of the AlN lead to a large number of microcracks, as shown in Fig. 6(e) (f). The depletion of Al element on the cross-section (up to approximately $1200 \mu\text{m}$ at 750°C), mainly due to the dissolution of loosely corroded AlN grains [34,35], which result in an undulating corrosion

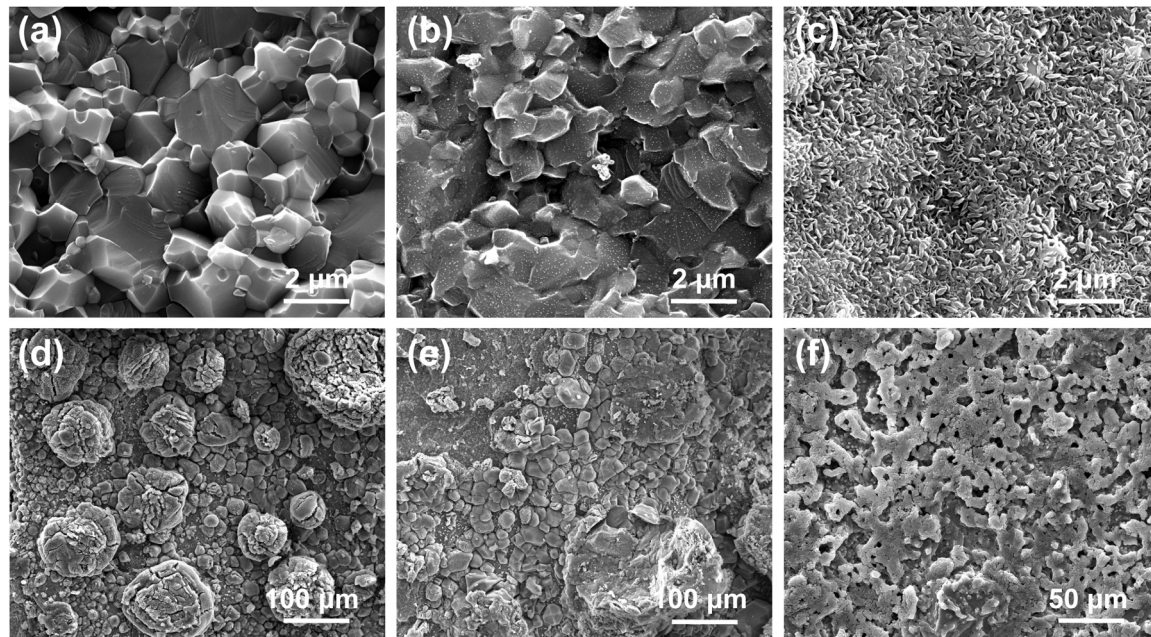


Fig. 4. Surface morphologies of AlN layer before and after exposure to the Li/LiF-LiCl-LiBr vapor at varied temperatures for 100 h. (a) before exposure, (b) 550°C , (c) 600°C , (d) 650°C , (e) 700°C , and (f) 750°C .

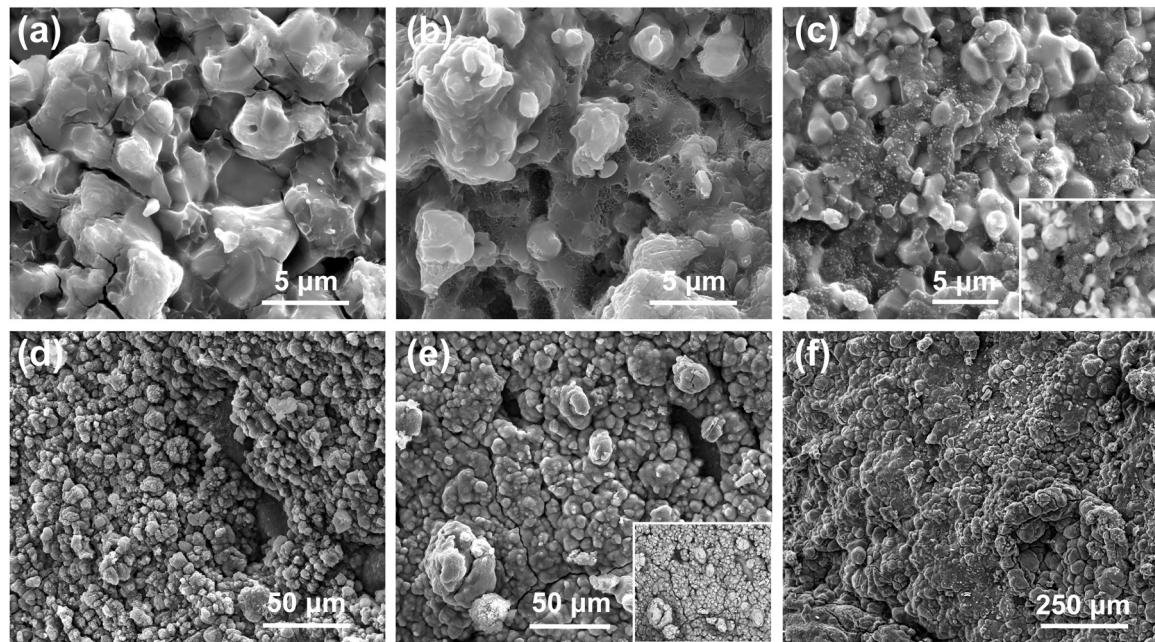


Fig. 5. Surface morphologies of AlN/Mo layer before and after exposure to the Li/LiF-LiCl-LiBr vapor at varied temperatures for 100 h. (a) before exposure, (b) 550 °C, (c) 600 °C, (d) 650 °C, (e) 700 °C, and (f) 750 °C.

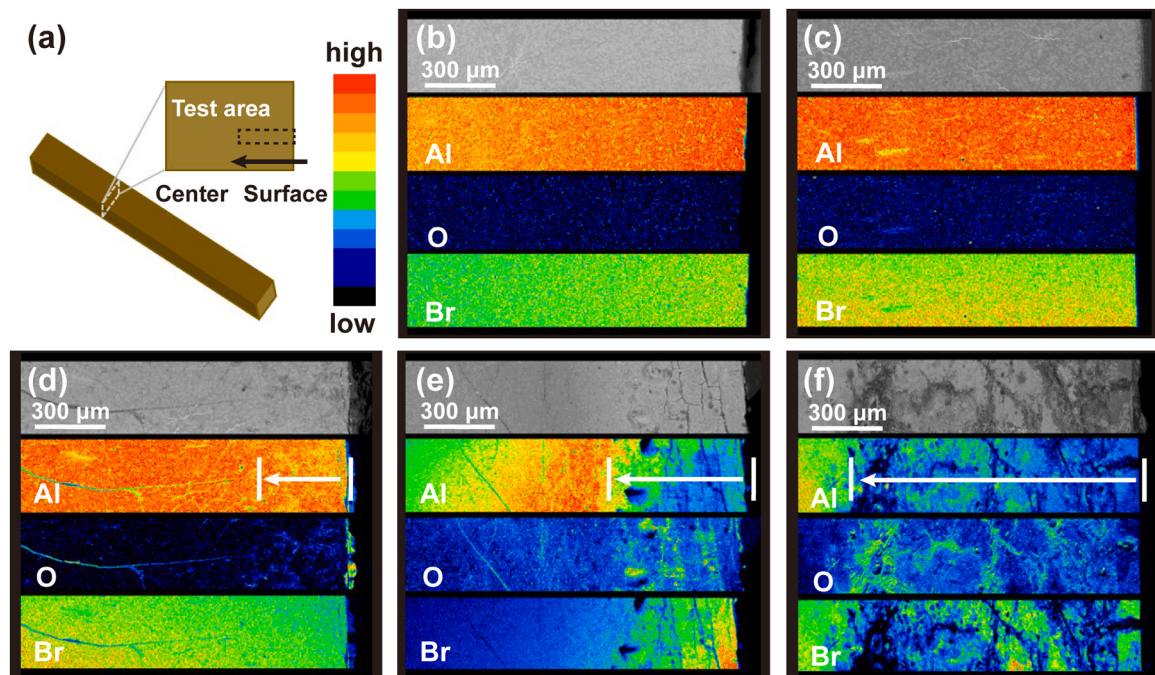


Fig. 6. The cross-sectional EPMA mapping of the AlN layer after exposure to the Li/LiF-LiCl-LiBr vapor at different temperatures for 100 h. (a) schematic diagram of selected area, (b) 550 °C, (c) 600 °C, (d) 650 °C, (e) 700 °C, and (f) 750 °C.

cross-section and reduces the detection sensitivity of the matrix element Al. It is worth noting that Li is too light to be detected within the Al-depleted area, and O is enriched in the microcracks. It is speculated that the distribution of O element indirectly represents the corrosion path of Li vapor due to the strong reducibility of Li and the strong thermodynamic driving force of the reaction between Li and O (Eq. (4-6)). Fig. 6(e) and (f) show that the Br element concentration fluctuates near the microcracks on the cross-section, suggesting that the halides are involved with the corrosion and enter the interior of the AlN, although its peaks are not detected on the surface through XRD.

However, the microstructure and elemental distribution of the AlN/Mo layer are barely changed after exposure to the Li/LiF-LiCl-LiBr vapor at varied temperatures for 100 h, as shown in Fig. 7. The depletion of the Al element is not found on the cross-section, and the elements of O and Br are not enriched on the cross-section. Fig. 7(e) shows the linear elemental distributions of the AlN/Mo layer from the surface to the interior after corrosion at 750 °C for 100 h, where a slight change in O and Br in a depth up to ~10 µm. Apparently, the corrosion resistance of the AlN/Mo layer under the Li/LiF-LiCl-LiBr vapor is superior to that of the AlN layer, and the corrosion damage to the AlN/Mo FGMS

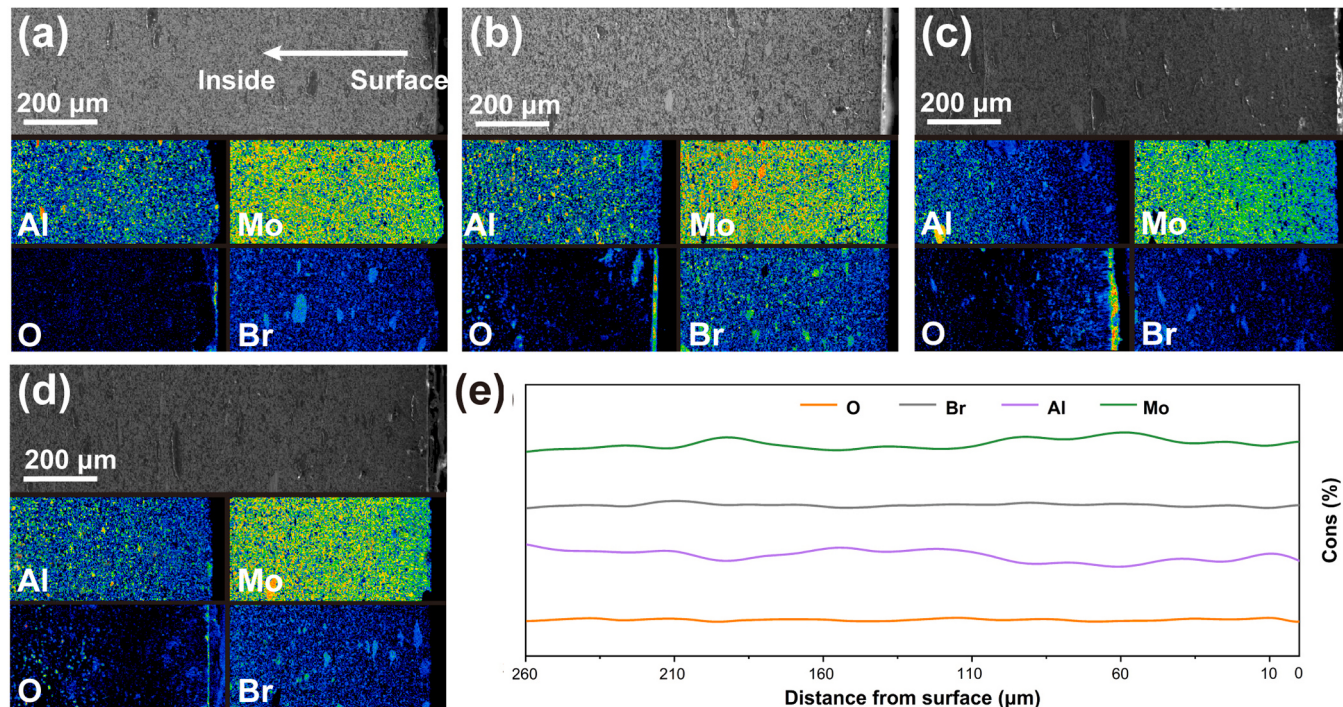


Fig. 7. The cross-sectional EPMA mapping of the AlN/Mo layer after exposure to the Li/LiF-LiCl-LiBr vapor at varied temperatures for 100 h. (a) 600 °C, (b) 650 °C, (c) 700 °C, (d) 750 °C, and (e) linear elemental distributions from surface to interior at 750 °C.

preferentially occurs in the AlN layer and the AlN-rich graded layers.

The analysis of morphologies and elemental distribution on the corroded cross-section plays an important role in unravelling corrosion mechanisms. The corroded AlN specimen of TEM, as shown in Fig. 8(b), is obtained with multistep milling processes by the lift-out FIB technique. SEM imaging of the milled slices shows the corrosion morphologies along the radial and axial directions (Fig. 8(c)). It is clear that the 3D pores exist inside the AlN layer after the corrosion in the Li/LiF-LiCl-LiBr vapor at 750 °C, and the size of the pores gradually decreases with increasing depths. The average diameters of the AlN grains and pores are ~2 μm and ~0.5 μm respectively, which indicates that the corrosive enters the AlN grains and leads to the disintegration of the AlN grains. In addition, the irregular corrosion channels on the cross-section imply that the Li/LiF-LiCl-LiBr vapor tends to diffuse along the grain boundaries, preferentially corroding the grain boundaries and then diffusing into adjacent AlN grains. The loose corrosion products in the corroded area are fractured during the Ga ion milling process, thereby forming the

channels and pores.

3.4. High-temperature corrosion mechanism

Despite the absence of any change in corrosion products (from 650 °C to 750 °C), performing TEM analysis on specimens corroded at higher temperatures proved instrumental in acquiring a comprehensive understanding of the corrosion mechanism. Subsurface TEM analysis of the AlN layer after exposure to the Li/LiF-LiCl-LiBr vapor for 750 °C/100 h (corresponding to Fig. 8(b)) is shown in Figs. 9 and 10. The EDS mapping presents that a small amount of yttrium aluminate induced by the Y₂O₃ additives is formed on the AlN grain boundaries. The microcracks caused by the corrosion-induced residual stresses are staggered along the AlN grain boundaries. The curved and blurred grain boundaries in the subsurface demonstrate that the dense AlN layer of tetrahedral grains becomes porous after corrosion, as shown in Fig. 9(b). In addition, the morphology of AlN grains was changed from regular tetrahedral to

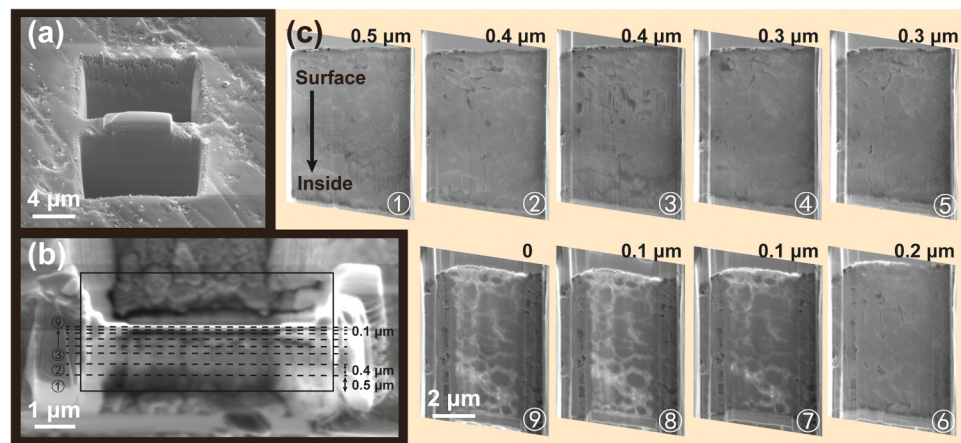


Fig. 8. SEM images of the FIB cutting process on the AlN layer corroded at 750 °C for 100 h. (a) protective Pt layer on the selected area, (b) specimen of TEM after multistep milling by Ga ions, (c) tiled 2D slices milled from (b).

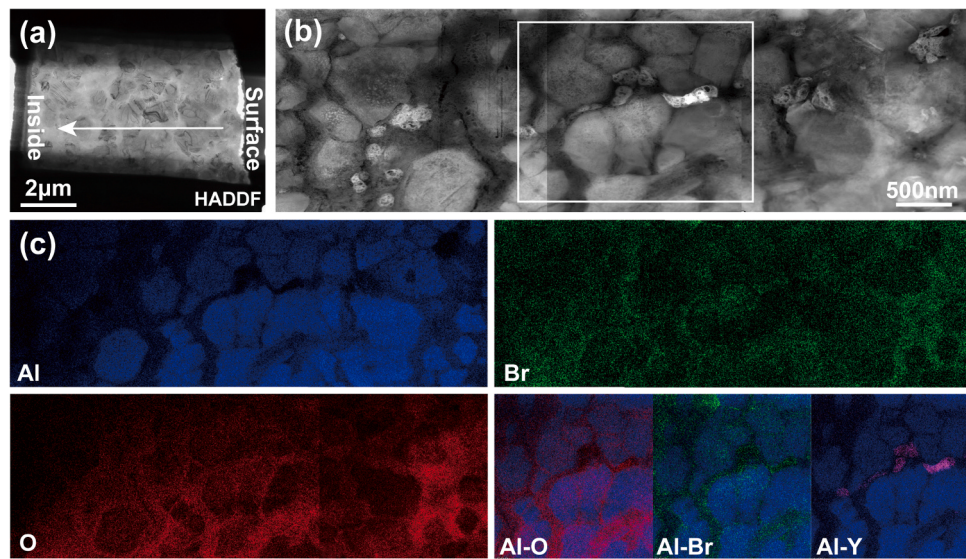


Fig. 9. TEM analysis of the AlN layer after exposure to the Li/LiF-LiCl-LiBr vapor at 750 °C for 100 h. (a) TEM imaging of the FIB-cut specimen, (b) corresponding magnified image of (a) from surface to interior, (c) corresponding EDS mappings of the Al, Br, and O elements in (b).

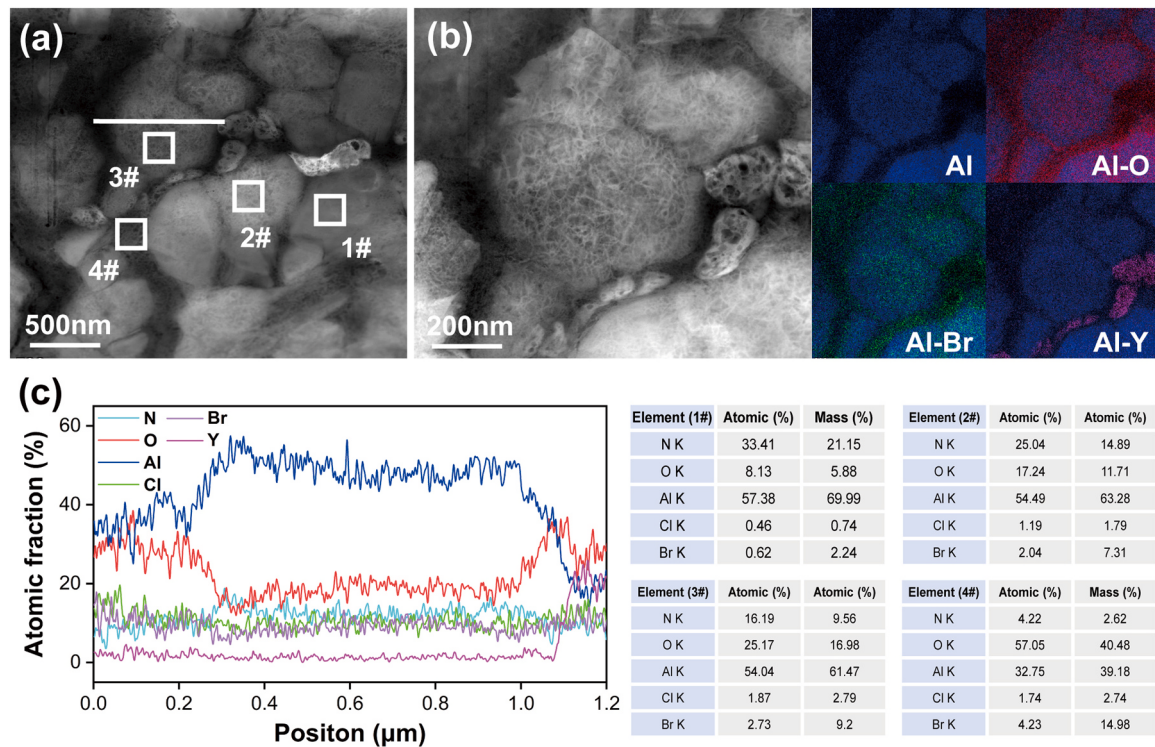


Fig. 10. TEM analysis of the AlN layer after exposure to the Li/LiF-LiCl-LiBr vapor at 750 °C for 100 h. (a) magnified image in Fig. 9(b), (b) corresponding magnified image and EDS mapping of 3# selected area in (a), (c) corresponding EDS elements line and point distributions in (a).

irregular circular and then disintegrated after exposure to the Li/LiF-LiCl-LiBr vapor at 750 °C (corresponding to Fig. 8(c)). It is evidenced from Fig. 9(c) that the elements of O and halogen, such as Br, dominate at the expanded AlN grain boundaries. Moreover, the elemental mapping of O and Br is consistent with the Al element, meaning that the Li/LiF-LiCl-LiBr vapor not only fills the AlN grain boundaries but also diffuses into the interior of the AlN grain after the high-temperature corrosion.

Fig. 10 shows the magnified images in Fig. 9(b) and the corresponding semi-quantitative analysis of each element in the selected area. The grain boundaries of AlN are filled with fluffy flocs, as well as a small

quantity of yttrium aluminate after the 750 °C corrosion in Li/LiF-LiCl-LiBr vapor (Fig. 10(b)). Notably, most of the AlN grains in the subsurface are also occupied by the flocs, whose compositions can provide important hints for understanding the corrosion mechanism. The compositions of selected areas 1–4# in Fig. 10(a) are compiled in Fig. 10(c). The chemical compositions of the AlN grain of 3# (Fig. 10(b)) are mainly Al (54.04 at%), O (25.17 at%), N (16.19 at%), and a small amount of Br (2.73 at%), Cl (1.87 at%). Compared to the selected areas 1–3#, the concentration of O in the AlN grain boundaries (4#) is much higher than that of other elements. Moreover, it seems that the concentration of O on the AlN grain surface is largely correlated with the flocs, and the

distribution of O element can indirectly represent the corrosion path of the Li/LiF-LiCl-LiBr vapor. It is suggested that the formation of flocs is attributed to the Li/LiF-LiCl-LiBr vapor corrosion.

All the results mentioned above demonstrate that elevated temperatures, particularly above 600 °C dominantly drive the corrosion and the resultant distortion of AlN layers under the Li/LiF-LiCl-LiBr vapor. According to the thermodynamic calculations, the phase transition and corrosion of the AlN layer are governed by the high-temperature Li vapor. By contrast, the LiF-LiCl-LiBr vapor does not promote the corrosion of the AlN while merely diffusing along the corrosion path. Li vapor first diffuses along the AlN grain boundaries during the corrosion process, expands the grain boundaries, and generates microcracks, as shown in Fig. 9(b). Meanwhile, amorphous flocs appear at the grain boundaries, as shown in Fig. 10(b) and Fig. 11(b), and gradually transfer to the adjacent AlN grains, which is proved by the curved boundaries between the amorphous and crystalline phase, as shown in Fig. 11(c) (d). Besides, under the excitation of transmitted electrons, polycrystalline diffraction rings gradually appear in the amorphous area caused by unstable LiOH crystallization [36,37]. The amorphous flocs formed after corrosion in Li/LiF-LiCl-LiBr vapor are composed of disintegrated AlN grains and corrosives (LiOH, halides).

To further investigate the corrosion mechanisms for the AlN/Mo layer at 750 °C, the subsurface TEM analysis is performed (see Figs. 12 and 13). In the AlN/Mo layer, the grains and grain boundaries of AlN maintain the morphology, and there is no flocs adhesion, indicating that the gradient Mo networks significantly inhibit the corrosion under the Li/LiF-LiCl-LiBr vapor. Fig. 12(c) shows that O element is mainly concentrated at the interfaces of AlN/Mo and AlN/AlN, and the diffusion depth at the subsurface is only ~10 μm, which is much lower than that in the AlN layer (~1200 μm). Interestingly, not all grain boundaries of the AlN/Mo layer are penetrated with O, and it depends on the bonding condition of the grain boundaries. Due to the differences in thermal expansion coefficient and wettability, the non-uniform forces during sintering and shrinkage lead to different bonding conditions (weak or strong bonding) between AlN and Mo grain boundaries [27]. It is found that O element tends to penetrate into the weakly bonded AlN/Mo grain boundaries. Fig. 13(a₁) shows that the amorphous AlN grain boundaries are formed after corrosion, while the semi-coherent AlN/Mo (Fig. 13(a₃) and Mo/Mo (Fig. 13(a₂) grain boundaries remain unchanged. This suggests that the strongly bonded AlN/Mo and Mo/Mo grain boundaries contribute to the desirable corrosion resistance compared to the AlN/AlN counterparts. Fig. 13(c) shows the chemical compositions at

spots 1–4# of the weakly bonded area in Fig. 13(b), where Al and Mo elements are dispersed at the grain boundary regions (2# and 3#), and only minor Mo is detectable within the AlN grain (4#). Notably, O is not detected in spots 1# and 4# that are located inside the Mo and AlN grains, respectively. By contrast, O contents at the AlN/Mo grain boundaries are 1.54 at% (2#), 41.32 at% (3#) respectively, which proves that the O is able to diffuse towards the AlN side with a shallow diffusion depth. Moreover, it is hard to detect the halogen elements (Cl, Br) at the AlN/Mo grain boundary, indicating that the molten salt could not penetrate along the grain boundaries in the AlN/Mo layer at 750 °C.

In terms of the distribution of O element, the corrosion path of the AlN/Mo layer after the 750 °C exposure under the Li/LiF-LiCl-LiBr vapor is governed by the weakly bonded AlN/Mo grain boundaries, as well as the AlN/AlN grain boundaries. The Mo significantly reduces the corrosion depth of the AlN/Mo layer due to the low diffusivity of the Li/LiF-LiCl-LiBr vapor along the Mo/Mo grain boundaries and within the Mo grains. The sealing performance of the AlN/Mo FGMS for the LMBs mainly depends on the corrosion resistance of the AlN layer and each AlN/Mo graded layer. When the operating temperature is lower than 600 °C, the AlN layer and the AlN/Mo graded layers offer excellent corrosion resistance, thus ensuring the long-term stability of the structure under the Li/LiF-LiCl-LiBr vapor condition. However, when the operating temperature of LMBs is over 600 °C, as shown in Fig. 14(a) and (b), the deformation of the AlN layer and each AlN/Mo graded layer is inconsistent due to the difference in corrosion resistance, resulting in stress concentration cracking of the AlN/Mo FGMS. Therefore, an operating temperature exceeding 600 °C is detrimental to the reliability of the AlN/Mo FGMS sealing component in LMBs.

This work takes advantage of FGMS to achieve superior corrosion resistance for the AlN ceramic and clearly underlines the operating temperature limit for the current LMBs employing functionally graded Mo/AlN/Mo seals. In addition, it is also promising to achieve the gradient joining of Mo/SS 304 using state-of-the-art additive manufacturing technologies that can produce FGMS inherently in the future work [38,39]. Employing such a FGM strategy should be favorable to obtain the quality and reliable packaging assembly for LMBs.

4. Conclusions

The high-temperature corrosion behavior of an AlN/Mo FGM exposed to the Li/LiF-LiCl-LiBr vapor was investigated in this study. The following conclusions can be drawn:

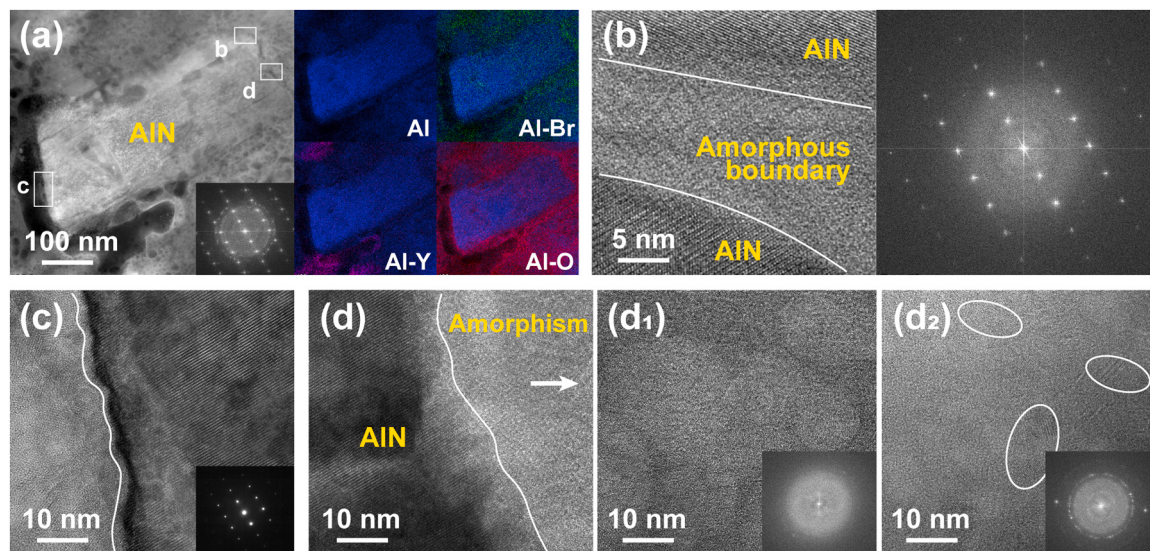


Fig. 11. (a) magnified TEM images and EDS mapping of AlN grain and grain boundaries in Fig. 9(b), (b) corresponding grain boundary and FFT pattern of selected area b in (a), (c) corresponding grain boundary and FFT pattern of selected area c in (a), (d) corresponding grain boundary of selected area d in (a).

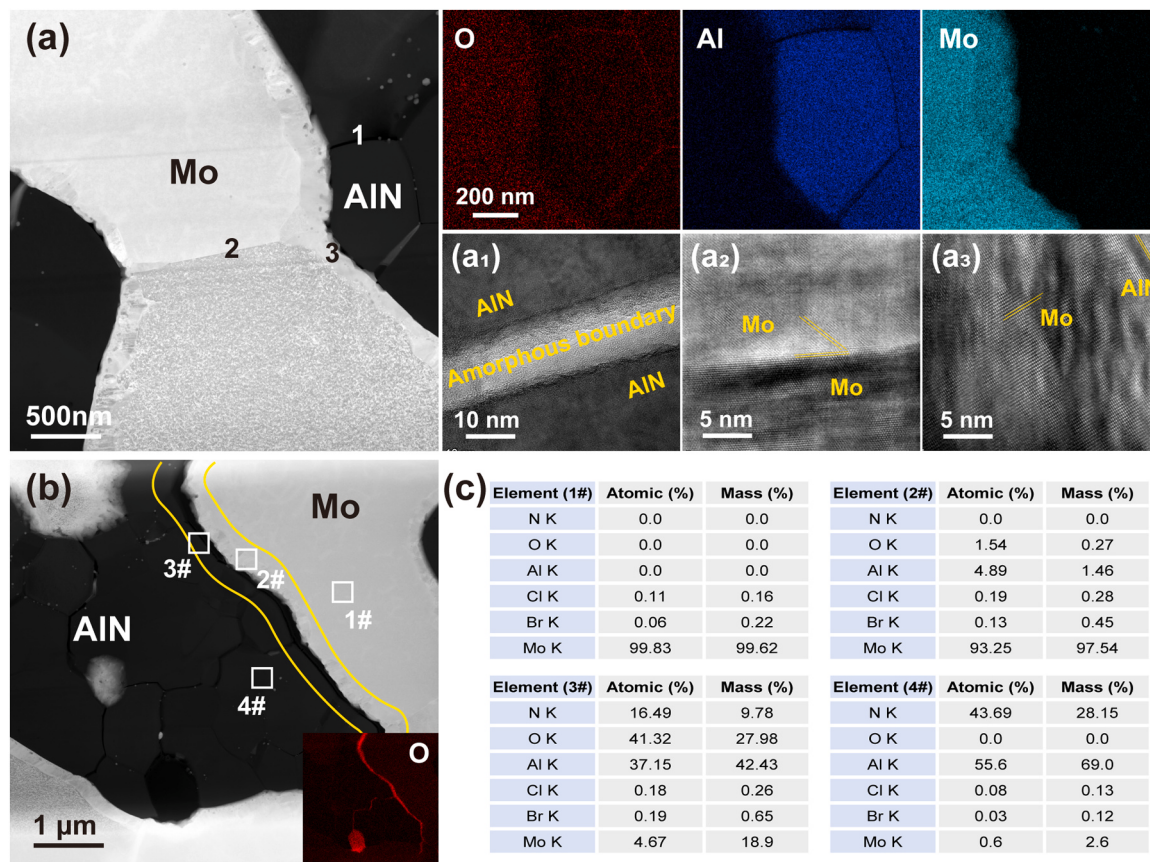


Fig. 13. (a-b) magnified TEM images and EDS mapping of AlN/Mo grain boundaries in Fig. 12(b). (c) corresponding EDS elements point distributions in (b).

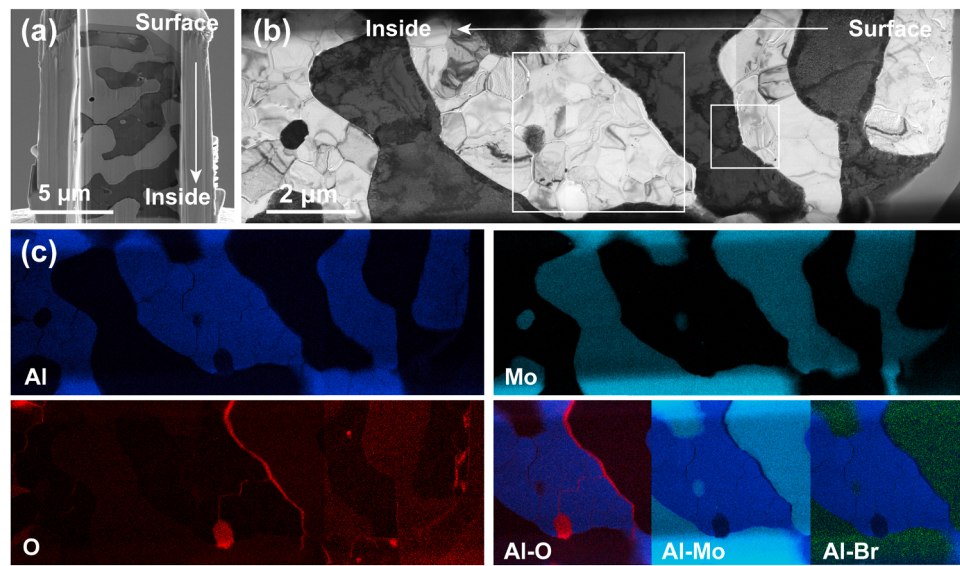


Fig. 12. (a-b) TEM images and (c) corresponding EDS mappings of the AlN/Mo layer after corrosion for 750 °C/100 h.

- (1) The corrosion failure of the AlN/Mo FGM occurred at 650 °C. The spatial corrosion depth in the AlN layer and AlN/Mo layers was largely dependent on the operating temperatures. After the exposure at 750 °C for 100 h, the corrosion depths of the AlN layer and AlN/Mo layer were 1200 μm and 10 μm, respectively.
- (2) Under the high-temperature Li/LiF-LiCl-LiBr vapor, the AlN was gradually disintegrated from the surface until it was severely distorted with no load-bearing capacity. The strong reducing Li

vapor firstly diffused along the grain boundary, which leads to cracks and amorphization, then gradually transferred to the adjacent AlN grains, forming a curved boundary between the amorphous zone and crystal grains.

- (3) The 3D networks of Mo significantly inhibited the corrosion, which was attributed to the low diffusivity of the Li/LiF-LiCl-LiBr vapor along the Mo/Mo grain boundaries and within the Mo grains. When the operating temperature of LMBs was above

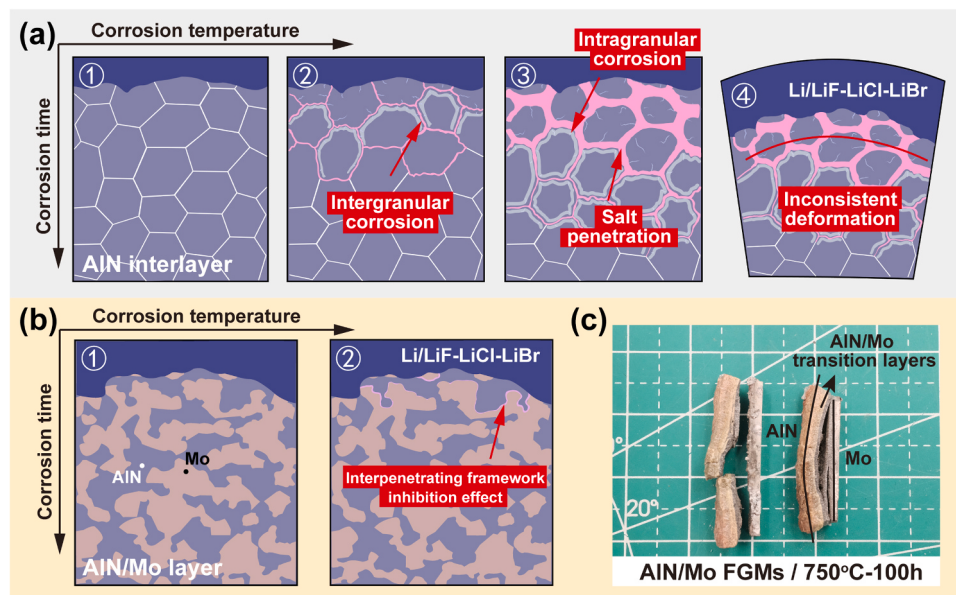


Fig. 14. Schematic diagram of corrosion mechanism of the Li/LiF-LiCl-LiBr vapor on AlN/Mo FGMs. (a) AlN interlayer, (b) AlN/Mo layer, (c) AlN/Mo FGMS.

600 °C, the inconsistent deformation of the AlN layer and AlN/Mo graded layers lead to the stress concentration induced cracking of the AlN/Mo FGM.

CRediT authorship contribution statement

Mingyong Jia: Methodology, Investigation, Writing-original draft, **Fei Chen:** Conceptualization, Resources, Funding acquisition, **Xipeng Tan:** Methodology, Writing - review & editing, Supervision, **Yaling He:** Formal analysis, Writing - review & editing, **Yueqi Wu:** Investigation, Formal analysis, **Qiang Shen:** Conceptualization, Supervision.

Declaration of Competing Interest

The authors declare that they have no known competing financial interests or personal relationships that could have appeared to influence the work reported in this paper.

Data availability

No data was used for the research described in the article.

Acknowledgments

This study is supported by the Guangdong Major Project of Basic and Applied Basic Research (2021B0301030001), the National Key Research and Development Program of China (2021YFA0716304), the Space Utilization System of China Manned Space Engineering (KJZ-YY-WCL03), the National Natural Science Foundation of China (No. 51972246 and 51521001), the Independent Innovation Projects of the Hubei Longzhong Laboratory (2022ZZ-32). Xipeng Tan acknowledges the funding support from NUS Start-up Grant (22-5928-A0001). Mingyong Jia acknowledges the funding support from China Scholarship Council (No. 202206950045).

References

- [1] D.J. Bradwell, H. Kim, A.H. Sirk, D.R. Sadoway, Magnesium-antimony liquid metal battery for stationary energy storage, *J. Am. Chem. Soc.* 134 (2012) 1895–1897.
- [2] H. Kim, D.A. Boysen, J.M. Newhouse, B.L. Spatocco, B. Chung, P.J. Burke, D. J. Bradwell, K. Jiang, A.A. Tomaszwoska, K. Wang, Liquid metal batteries: past, present, and future, *Chem. Rev.* 113 (2013) 2075–2099.
- [3] K. Wang, K. Jiang, B. Chung, T. Ouchi, P.J. Burke, D.A. Boysen, D.J. Bradwell, H. Kim, U. Muecke, D.R. Sadoway, Lithium-antimony-lead liquid metal battery for grid-level energy storage, *Nature* 514 (2014) 348–350.
- [4] X. Ning, S. Phadke, B. Chung, H. Yin, P. Burke, D.R. Sadoway, Self-healing Li-Bi liquid metal battery for grid-scale energy storage, *J. Power Sources* 275 (2015) 370–376.
- [5] S. Zhang, Y. Liu, Q. Fan, C. Zhang, T. Zhou, K. Kalantar-Zadeh, Z. Guo, Liquid metal batteries for future energy storage, *Energy Environ. Sci.* 14 (2021) 4177–4202.
- [6] T. Ouchi, D.R. Sadoway, Positive current collector for Li||Sb-Pb liquid metal battery, *J. Power Sources* 357 (2017) 158–163.
- [7] X. Zhou, H. Zhou, S. Yan, Y. He, W. Zhang, H. Li, K. Wang, K. Jiang, Increasing the actual energy density of Sb-based liquid metal battery, *J. Power Sources* 534 (2022), 231428.
- [8] H. Li, H. Yin, K. Wang, S. Cheng, K. Jiang, D.R. Sadoway, Liquid metal electrodes for energy storage batteries, *Adv. Energy Mater.* 6 (2016) 1600483.
- [9] G. Comino, S. Arrigoni, M. Apostolo, M. Albano, V. Arcella, New peroxide curable perfluoroelastomer for high temperature applications, *Prog. Rubber Plast. Recycl. Technol.* 17 (2001) 101–112.
- [10] B. Ameduri, B. Boutevin, Update on fluoroelastomers: from perfluoroelastomers to fluorosilicones and fluorophosphazenes, *J. Fluor. Chem.* 126 (2005) 221–229.
- [11] Z. Wen, Y. Hu, X. Wu, J. Han, Z. Gu, Main challenges for high performance Na-S battery: materials and interfaces, *Adv. Funct. Mater.* 23 (2013) 1005–1018.
- [12] M. Nicholas, R. Crispin, Diffusion bonding stainless steel to alumina using aluminium interlayers, *J. Mater. Sci.* 17 (1982) 3347–3360.
- [13] Q. Liu, Z. Wang, W. Liu, H. Yin, Z. Tang, Y. Qian, Ni-Mo-Cr alloy corrosion in molten NaCl-KCl-MgCl₂ salt and vapour, *Corros. Sci.* 180 (2021), 109183.
- [14] X. Lai, H. Yin, Z. Yang, Z. Tang, Synergistic effect of Cl⁻ and F⁻ on the corrosion behavior and mechanism of 316 stainless steel in NaNO₃ based molten salts and vapor, *J. Energy Storage* 65 (2023), 107243.
- [15] M. Nagura, M. Kondo, A. Suzuki, T. Muroga, T. Terai, Experimental study on corrosion of ceramic materials in natural convection lithium loop, *Fusion Sci. Technol.* 52 (2007) 630–634.
- [16] W. Lu, J. Wang, W. Pu, K. Li, W. Wang, S. He, D. Chu, J. Yang, Y. Zhu, Corrosion resistance of ceramic candidates for tritium permeation barriers exposed to molten lithium, *Corros. Sci.* 160 (2019), 108172.
- [17] K. Natesan, C. Reed, D. Rink, R. Haglund, Development and performance of aluminum nitride insulating coatings for application in a lithium environment, *J. Nucl. Mater.* 258 (1998) 488–494.
- [18] B. Pint, L. Chitwood, J. Di Stefano, Long-term stability of ceramics in liquid lithium, *J. Nucl. Mater.* 289 (2001) 52–56.
- [19] B. Pint, J. DeVan, J. Di Stefano, Temperature limits on the compatibility of insulating ceramics in lithium, *J. Nucl. Mater.* 307 (2002) 1344–1350.
- [20] B. Li, B. Wen, H. Chen, W. Zhang, X. Meng, M. Jia, F. Chen, Corrosion behaviour and related mechanism of lithium vapour on aluminium nitride ceramic, *Corros. Sci.* 178 (2021), 109058.
- [21] J. Zhang, J. Huang, R. Liu, G. Luo, Q. Shen, Corrosion behaviour of AlN ceramics in LiF-LiCl-LiBr-Li molten salt at 500 °C, *Corros. Sci.* 190 (2021), 109672.
- [22] A. Kara-Slimane, D. Juve, E. Leblond, D. Treheux, Joining of AlN with metals and alloys, *J. Eur. Ceram. Soc.* 20 (2000) 1829–1836.
- [23] A. Belyakov, I. Kuznetsova, R.Y. Kuftyrev, L. Pilavova, V. Seregin, Metallization of aluminum nitride ceramic, *Glass Ceram.* 69 (2012) 270–273.
- [24] B. Kieback, A. Neubrand, H. Riedel, Processing techniques for functionally graded materials, *Mater. Sci. Eng. A* 362 (2003) 81–106.

- [25] M. Naebe, K. Shirvanimoghaddam, Functionally graded materials: a review of fabrication and properties, *Appl. Mater. Today* 5 (2016) 223–245.
- [26] F. Chen, M. Jia, Y. She, Y. Wu, Q. Shen, L. Zhang, Compounds, mechanical behavior of AlN/Mo functionally graded materials with various compositional structures, *J. Alloy. Compd.* 816 (2020), 152512.
- [27] M. Jia, F. Chen, Y. Wu, L. Xu, Q. Shen, N. Jiang, J. Sun, Microstructure and shear fracture behavior of Mo/AlN/Mo symmetrical compositionally graded materials, *Mater. Sci. Eng. A* (2022), 142591.
- [28] G. Chen, L. Xue, J. Wang, Z. Tang, X. Li, H. Dong, Investigation of surface modifications for combating the molten aluminum corrosion of AISI H13 steel, *Cerros. Sci.* 174 (2020), 108836.
- [29] E. Hagen, Y. Yu, T. Grande, R. Høier, M. Einarsrud, Sintering of AlN using CaO-Al₂O₃ as a sintering additive: chemistry and microstructural development, *J. Am. Ceram. Soc.* 85 (2002) 2971–2976.
- [30] X. He, F. Ye, H. Zhang, L. Liu, Study of rare-earth oxide sintering additive systems for spark plasma sintering AlN ceramics, *Mater. Sci. Eng. A* 527 (2010) 5268–5272.
- [31] H.M. Lee, D.K. Kim, High-strength AlN ceramics by low-temperature sintering with CaZrO₃-Y₂O₃ co-additives, *J. Eur. Ceram. Soc.* 34 (2014) 3627–3633.
- [32] J. Qiu, Y. Hotta, K. Watari, K. Mitsuishi, M. Yamazaki, Low-temperature sintering behavior of the nano-sized AlN powder achieved by super-fine grinding mill with Y₂O₃ and CaO additives, *J. Eur. Ceram. Soc.* 26 (2006) 385–390.
- [33] D. Huang, Z. Tian, W. Cui, L. Gao, Z. Liu, X. Diao, G. Liu, Effects of Y₂O₃ and yttrium aluminates as sintering additives on the thermal conductivity of AlN ceramic substrates, *Ceram. Int.* 44 (2018) 20556–20559.
- [34] O. Muránsky, C. Yang, H. Zhu, I. Karatchevtseva, P. Sláma, Z. Nový, L. Edwards, Molten salt corrosion of Ni-Mo-Cr candidate structural materials for Molten Salt Reactor (MSR) systems, *Cerros. Sci.* 159 (2019), 108087.
- [35] W. Kim, S. Kwon, S. Cho, J. Lee, Effect of the grain size of YSZ ceramic materials on corrosion resistance in a hot molten salt CaCl₂-CaF₂-CaO system, *Cerros. Sci.* 170 (2020), 108664.
- [36] R. Black, S.H. Oh, J.H. Lee, T. Yim, B. Adams, L.F. Nazar, Screening for superoxide reactivity in Li-O₂ batteries: effect on Li₂O₂/LiOH crystallization, *J. Am. Ceram. Soc.* 134 (2012) 2902–2905.
- [37] J. Lu, Y. Lei, K.C. Lau, X. Luo, P. Du, J. Wen, R.S. Assary, U. Das, D.J. Miller, J. W. Elam, A nanostructured cathode architecture for low charge overpotential in lithium-oxygen batteries, *Nat. Commun.* 4 (2013) 1–10.
- [38] X.P. Tan, Y. Kok, Y.J. Tan, M. Descoings, D. Mangelinck, S.B. Tor, K.F. Leong, C. K. Chua, Graded microstructure and mechanical properties of additive manufactured Ti-6Al-4V via electron beam melting, *Acta Mater.* 97 (2015) 1–16.
- [39] S.H. Li, P. Kumar, S. Chandra, U. Ramamurti, Directed energy deposition of metals: processing, microstructures, and mechanical properties, *Int. Mater. Rev.* (2022) 1–43.